Influence of ion energy and ion species on ion channeling in $LiNbO_3$

T. Steinbach, F. Schrempel, Th. Gischkat, and W. Wesch
Institut für Festkörperphysik, Friedrich-Schiller-Universität Jena, Max-Wien-Platz 1, D-07743 Jena, Germany
(Received 24 July 2008; revised manuscript received 21 October 2008; published 12 November 2008)

Ion irradiation of $LiNbO_3$ causes the formation of defects due to nuclear as well as electronic energy deposition ϵ_n and ϵ_e, respectively. However, the defect formation is influenced by the orientation of the crystal. If the irradiation is performed along a low index crystallographic direction (on-axis) the defect distributions are strongly affected by ion channeling because the ions are prevented from close collisions with the target atoms so that the penetration range of the impinging ions is increased. In order to investigate the effect of ϵ_n and ϵ_e on damage formation $LiNbO_3$ crystals were irradiated on- and off-axes using Si^+ and Cu^+ ions with energies ranging from 550 keV to 2 MeV. We demonstrate for on-axis irradiation that at low ion energies where ϵ_n dominates the formation of defects, the defect distribution is shifted to larger depths compared to off-axis irradiation. The investigation of the shift shows a square-root dependence on both ion energy and ion species. Furthermore, on-axis irradiation was done using high-ion energies where defects are formed in the near-surface region due to electronic energy loss. Compared to off-axis irradiation a thinner amorphous surface layer was formed as a result of the reduced electronic energy loss in the case of on-axis irradiation. For on-axis irradiation ϵ_e could be estimated in two different ways considering the layer thickness and the penetration range of the incident ions.

DOI: 10.1103/PhysRevB.78.184106 PACS number(s): 61.85.+p, 77.84.Dy, 61.80.Jh, 42.70.Mp

I. INTRODUCTION

The patterning of electro-optical materials is of increasing interest for the engineering of photonic devices such as electrical tunable filters and switches. Moreover, resonant elements in nonlinear optical materials may possess transmission and reflection depending on the intensity of light. Due to its physical properties, such as large electro-optical and nonlinear optical coefficients, lithium niobate ($LiNbO_3$) (Ref. 1) is an important material for the fabrication of integrated optical devices. However, the high-chemical resistance of $LiNbO_3$ demands specific patterning techniques.[2–10]

A promising method to pattern $LiNbO_3$ is the use of ion irradiation and subsequent wet chemical etching [ion-beam enhanced etching (IBEE)].[11–17] In this process the physical properties of $LiNbO_3$ such as the refractive index, the etching behavior, the chemical stability, and the density are modified due to the radiation damage, which can be attributed to both nuclear and electronic energy losses of the incident ions.[11–22]

Normally the ion irradiation is done in random direction (off-axis), which necessarily results in patterns not aligned with the crystal axis.[16,17] However, a number of applications demand patterns aligned with a certain crystallographic axis (e.g., to get phase matching). To realize such structures the irradiation has to be performed along the corresponding axis (on-axis). As a consequence of on-axis irradiation ion channeling occurs (channeling effect).[23–26] Hence, compared to off-axis irradiation, the projected range of the ions increases because the channeled ions are prevented from close collisions with the target atoms. As a result the defect distribution is shifted to larger depths and less defects are created in the case of on-axis compared to off-axis irradiation, which has already been demonstrated in previous channeling experiments in silicon,[26–29] silicon carbide,[30] and recently $LiNbO_3$.[31]

Understanding the influence of the channeling effect in $LiNbO_3$ is essential to successfully apply the IBEE method. The purpose of the paper is to present experimental results dealing with the shift of the defect maximum to larger depths depending on ion energy and ion species (Si^+ and Cu^+ ions). Furthermore, on-axis irradiation was done in an energy range where defect formation due to electronic energy loss occurs. However, for irradiation under channeling conditions the electronic energy deposition is reduced compared to the corresponding off-axis irradiation. The comparison of both irradiation conditions offers the possibility to estimate the electronic energy deposition for on-axis irradiation by two different ways considering the layer thickness and the penetration range of the incident ions.

II. EXPERIMENT

Commercial x-cut ($[11\bar{2}0]$) congruent $LiNbO_3$ crystals were irradiated with Si^+ and Cu^+ ions with energies in the range of 550 keV and 2 MeV. The samples were kept at room temperature and the irradiation was performed at tilt angles of 0° (on-axis) and 7° (off-axis) with respect to the crystal axis. The tilting plane was rotated to avoid planar channeling during off-axis irradiation. Ion fluences were 3×10^{14} and 7×10^{13} cm^{-2} for Si^+ and Cu^+ ions, respectively. These fluences were chosen to achieve comparable defect concentrations in the maximum of the defect distribution for both ion species. The depth distributions of the nuclear ϵ_n as well as the electronic ϵ_e energy deposition were calculated using SRIM-2006.[32]

Rutherford backscattering spectrometry (RBS) in channeling configuration with 1.8 MeV H^+ ions was applied to analyze the damage accumulation. The number of Nb atoms displaced from their crystal lattice sites were taken as a measure for the total amount of the damage caused by irradiation. From the Nb part of the RBS spectra, the relative con-

centration of displaced lattice atoms $n_{da}(z)$ was calculated using the computer code DICADA, which is based on the discontinuous model of dechanneling.[33,34] In the following n_{da} is referred to as defect concentration, whereas $n_{da}=0$ and 1 correspond to perfect and amorphous crystals, respectively.

All experiments were performed in a chamber allowing stepwise ion implantation and subsequent RBS analysis without removing the sample. To achieve good channeling conditions the irradiation was carried out through two apertures forming an irradiated spot of 3 mm. For RBS measurements a collimator was brought in the course of the beam for analyzing solely the central part of the irradiated spot with a diameter of 1 mm. These conditions guarantee a beam divergence less than 0.1° and a homogeneous fluence distribution within the analyzed spot. The orientation of all samples, i.e., the corresponding axial direction, with respect to the ion beam was determined by angular scan measurements with 1.8 MeV H^+ ions. Thereby, the samples were mounted on a three axis goniometer having an angular accuracy of 0.01°.

Subsequent to the irradiation, the samples were etched stepwise in a hydrofluoric (HF) solution of 3.7 and 40% at a temperature of 40 °C, respectively. The etched depth was measured relative to the nonetched surface after each etch step with a Sloan DEKTAK surface profilometer. The etching rates as a function of the depth z were received by stepwise etching.

III. EXPERIMENTAL RESULTS

A. RBS results

Figure 1 shows the relative defect concentration $n_{da}(z)$ as a function of the depth z obtained from the RBS measurements for on- and off-axis irradiations of x-cut $LiNbO_3$ using Si^+ ions with different energies. In Fig. 1(c) the depth distributions of the energy transfer to ionization (electronic energy deposition ϵ_e) as well as to displacements (nuclear energy deposition ϵ_n) are included for the example of Si^+ irradiation of $LiNbO_3$ with an ion energy of 1 MeV.

For off-axis irradiation (open symbols), the defect maxima are located in depth regions of the nuclear energy loss, which becomes apparent in Fig. 1(c). The maximum of ϵ_n is located in a depth of 650 nm and the shape of the defect profile is coincident with the calculated distribution of ϵ_n.

There are two essential differences between on- and off-axis irradiations. On one hand, the maxima of the defect distributions for on-axis irradiation (closed symbols) are shifted to larger depths compared to that for off-axis irradiation (see Table I). On the other hand, less defects are created for the same ion fluence in the case of on-axis irradiation. Especially the surface of the crystal is nearly free of defects for all on-axis irradiation. However, in Fig. 1 it is obvious that the defect concentration does not fall to zero for both irradiation conditions at larger depths. This can be accounted for by the presence of a low concentration of correlated defects (e.g., stacking faults or dislocations) which are disregarded by the calculation of defect profiles with DICADA because only uncorrelated lattice defects are taken into consideration for the calculation.

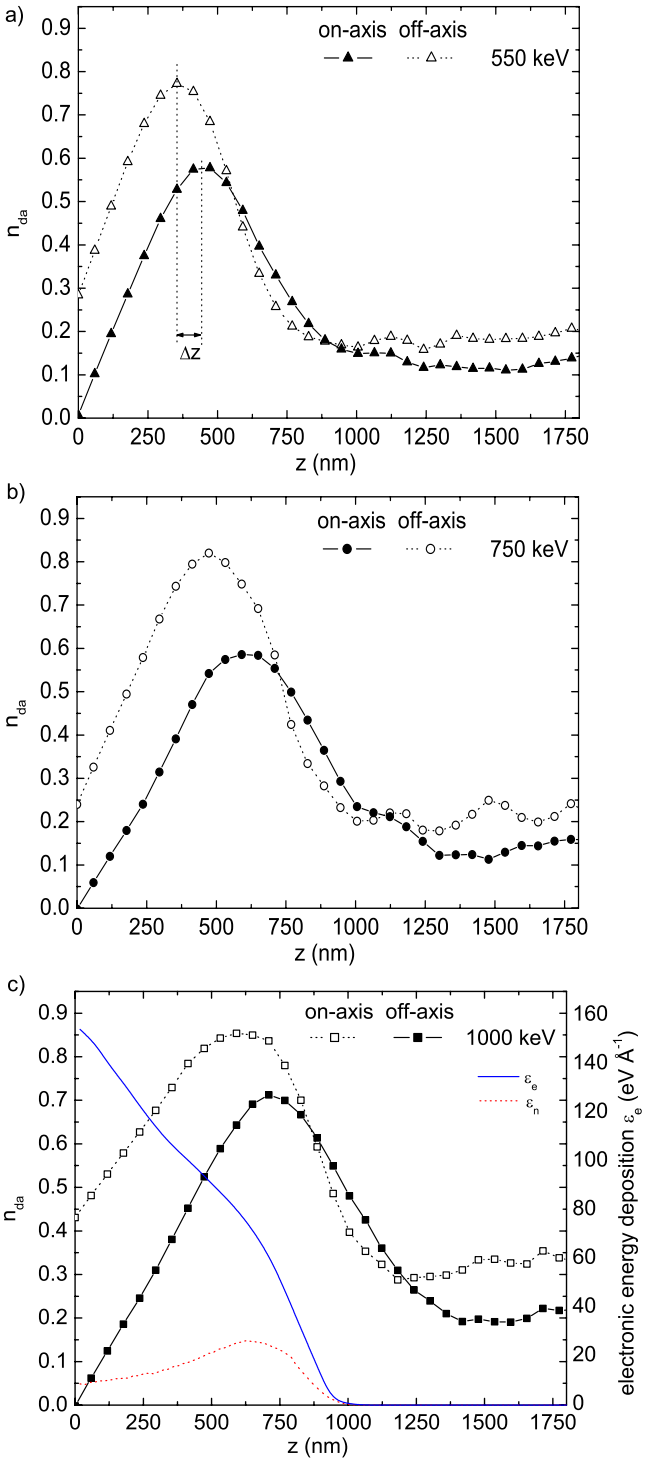

FIG. 1. (Color online) Relative defect concentration n_{da} versus depth z calculated from the Nb part of the RBS spectra for x-cut $LiNbO_3$ irradiated with (a) 550, (b) 750, as well as (c) 1000 keV Si^+ ions. The irradiation was carried out at an ion fluence of 3×10^{14} cm^{-2}. The beam orientation is represented by open (off-axis) and closed (on-axis) symbols, respectively. SRIM calculation of electronic ϵ_e and nuclear ϵ_n energy deposition versus depth z for $LiNbO_3$ irradiated with 1 MeV Si^+ ions are included in (c).

In Fig. 2 the relative defect concentrations are shown as a function of the depth for x-cut $LiNbO_3$ irradiated with Si^+ ions with ion energies of 1.0, 1.25, 1.5, and 2.0 MeV, respec-

TABLE I. Shift of the maximum of the defect distribution Δz as well as the electronic energy deposition ϵ_e at the surface for the irradiation of x-cut $LiNbO_3$ with Si^+ and Cu^+ ions of various energies at an ion fluence of 3×10^{14} and 1×10^{14} cm^{-2}, respectively.

Ion	E_{ion} (keV)	ϵ_e (eV Å^{-1})	Δz (nm)
	No surface damage		
Cu^+	1000	124	165 ± 10
	1400	145	205 ± 10
Si^+	550	100	95 ± 5
	750	126	115 ± 10
	1000	153	125 ± 10
	With surface damage		
	1250	180	120 ± 10
	1500	202	95 ± 15
	2000	250	25 ± 10

tively. Similarly to irradiation with 1 MeV (see above), the 1.25 MeV on-axis irradiation (closed circles) shows a nearly undamaged surface layer and the defect maximum is formed in the maximum of the nuclear energy deposition. By contrast, apart from the damage peak caused by nuclear energy loss an increased defect concentration at the surface of the crystal ($n_{da}=0.8$) is obtained for off-axis irradiation (open circles).

This second defect maximum cannot be explained by nuclear collision damage since no correlation is established with the nuclear stopping curve [cf. Fig. 1(b)]. Hence, the increased damage at the surface must be a consequence of the increasing influence of the electronic energy deposition of $\epsilon_e=180$ eV Å^{-1} at the surface [compared to $\epsilon_e=153$ eV Å^{-1} at 1 MeV (see Table I)]. Apparently, the electronic energy deposition exceeds a material-specific threshold for damage formation (cf. Sec. IV C).

With further increasing ion energy, 1.5 and 2 MeV [see Fig. 2(b)], respectively, for off-axis irradiation a continuous increase in the surface damage is obtained ($n_{da}=1$) and a strong damaged layer has extended into the crystal (open diamonds). The electronic energy deposition increases from $\epsilon_e=202$ to 250 eV Å^{-1} for an ion energy of 1.5 and 2 MeV, respectively.

In contrast, only a weak-damaged near-surface region is formed in case of 1.5 MeV on-axis irradiation ($n_{da}=0.1$). For on-axis irradiation a strongly damaged surface layer ($n_{da}=1$) is only obtained by irradiation with an ion energy of 2 MeV (closed diamonds). For both, 2 MeV on-axis and off-axis irradiations (diamonds), finally, a damaged layer is obtained extending from the surface to a depth of about 1250 nm. Note that on-axis compared to off-axis irradiation shows a lower defect concentration and both defect distributions have a minimum at about 600 nm. Similar to the off-axis irradiation, the near-surface damage has to be attributed to the increased influence in the electronic energy deposition. However, for on-axis irradiation the formation of defects near the surface starts at higher-ion energies compared to off-axis irradiation.

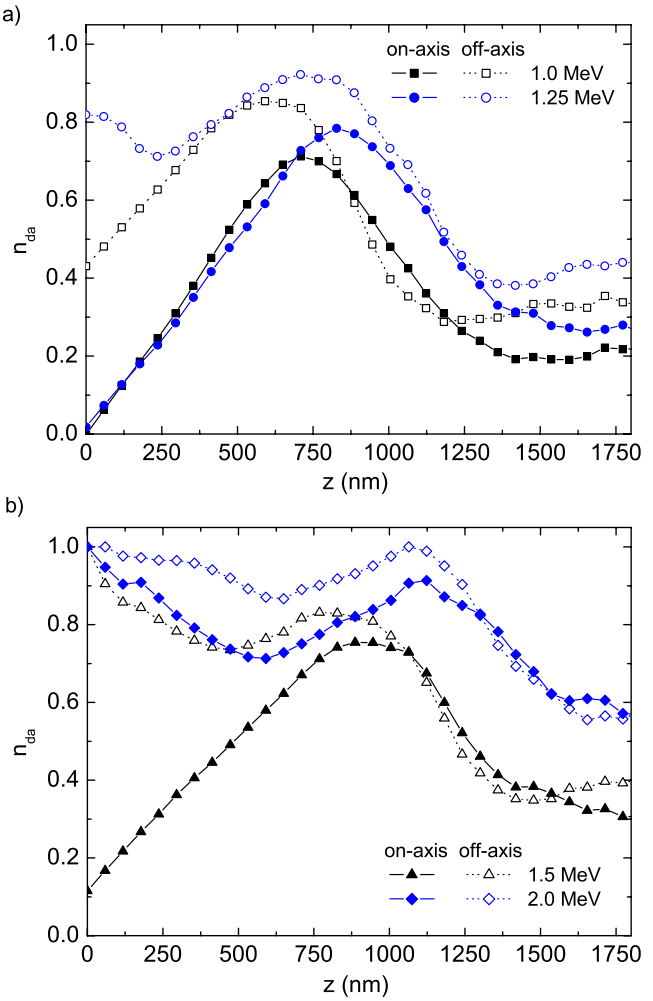

FIG. 2. (Color online) Relative defect concentration n_{da} versus depth z for x-cut $LiNbO_3$ irradiated with Si^+ ions with ion energies of 1 MeV (squares), 1.25 MeV (circles), 1.5 MeV (triangles), and 2 MeV (diamonds). The fluences amount to 3×10^{14} cm^{-2}. On-axis irradiation is represented by closed symbols and off-axis irradiation by open symbols, respectively.

In Table I the measured peak shifts Δz, i.e., the difference of the depth of the defect maxima for on- and off-axis irradiations, are summarized for all ion species and ion energies used for the irradiation. The errors of Δz represent the degree of uncertainty in the determination of the position of the defect maxima for on- and off-axis irradiations (cf. Figs. 1 and 2). Additionally, the electronic energy deposition at the surface of the crystal is listed. Obviously, if the nuclear energy deposition dominates the defect formation the peak shift increases with increasing ion energy (cf. Sec. IV B, Fig. 4). Considering the peak shift for Si^+ ions with $E>1$ MeV, i.e., if an increased defect concentration is observed at the surface in the RBS spectra, a decrease in Δz with increasing ion energy turns out (cf. Sec. IV C, Fig. 5).

For an ion energy of 1 MeV the comparison between Si^+ and Cu^+ ions shows that the peak shift is clearly swayed by the ion mass too (spectra not shown).

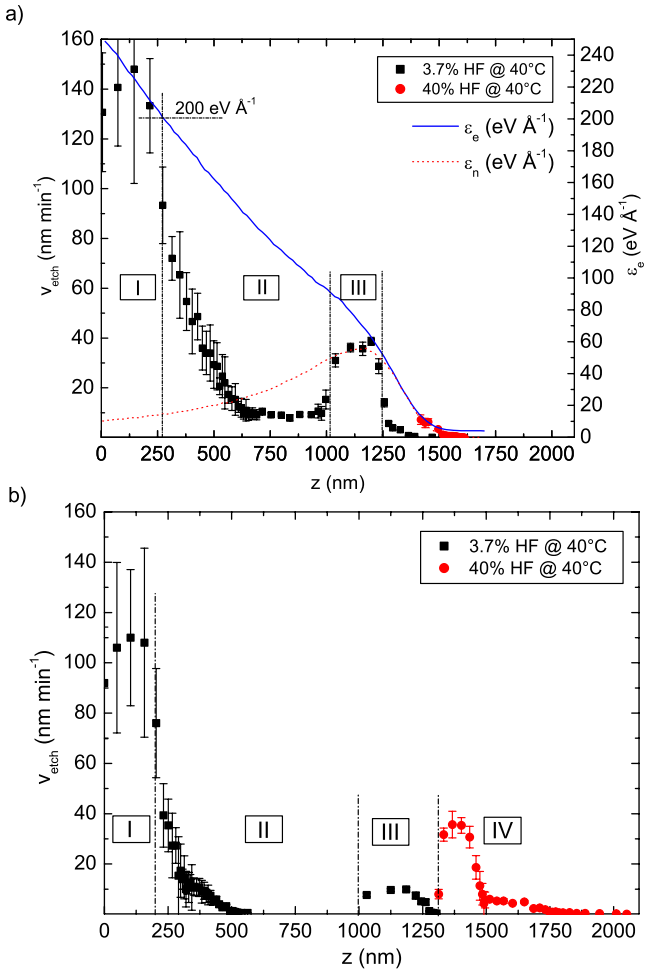

FIG. 3. (Color online) Etching rate v_{etch} as a function of depth z obtained for x-cut $LiNbO_3$ irradiated (a) off- and (b) on-axes with 2 MeV Si^+ ions and etched at 40 °C in a HF solution of 3.7 and 40%, respectively. The error bars indicate the standard error of the mean for up to five measurements of the step height at five different locations of the surface. The nuclear ϵ_n as well as the electronic ϵ_e energy deposition calculated with SRIM-2006 are included in (a).

B. Etching results

As an example, the etching rate is plotted in Fig. 3 as a function of the depth z for off-axis (a) and on-axis (b) irradiations with 2 MeV Si^+ ions.

According to the depth distribution of the defect concentration [cf. Fig. 2(b)] the depth distribution of the etching rate of the off-axis irradiation [Fig. 3(a), 3.7% HF solution] can also be divided into three areas: the first area (I) extending from the surface to a depth of 275 nm is characterized by an average etching rate of 138 nm min^{-1}. At larger depths the etching rate decreases rapidly and the second area (II) shows a constant etching rate in a depth between 600 and 1000 nm (v_{etch}=10 nm min^{-1}). In a depth between approximately 1000 and 1300 nm the third area (III) is obtained with an average etching rate of 35 nm min^{-1}. These areas refer to three various strongly damaged crystal areas, which are already indicated in the damage profiles [cf. Fig. 2(b)] as stated above. However, the areas II and III are only rudimentary reflected in the defect distribution because the defect profile shows a higher defect concentration. In accordance to previous studies[16] the obtained etching rates indicate that the surface layer (area I) is amorphous, whereas the buried damaged layer (area III) is not amorphous. Additionally, in Fig. 3(a) the electronic and the nuclear energy losses are plotted.

The areas I–III appear for on-axis irradiation too [cf. Fig. 3(b)]. However, the etching rate is lower compared to off-axis irradiation. The first area extending from the surface to 200 nm is smaller compared to off-axis irradiation and shows an average etching rate of 100 nm min^{-1}. Subsequently, the etching rate decreases rapidly and is almost zero at a depth of 600 nm. The etching rate of the third area (from 1000 to 1300 nm) amounts to 10 nm min^{-1}. To bridge the gap between 600 and about 1000 nm the sample was etched a few minutes in 40% HF solution (not shown) because the etching rate is higher for the same defect concentration due to the higher HF concentration.[35]

Additionally, for on-axis irradiation and subsequent etching in 40% HF solution a fourth area (IV) can be determined [Fig. 3(b), circles]. Again, due to the higher HF concentration the etching rate is higher for the same defect concentration (approximately 35 nm min^{-1}). At a depth of 1450 nm the etching rate decreases with increasing depth, i.e., with decreasing defect concentration. The maximum etched depth z^C_{max} amounts to 2060 nm and is increased by a factor of 1.3 compared to off-axis irradiation.

IV. DISCUSSION

A. Channeling irradiation

The reduced defect concentration as well as the shift of the damage peak for on-axis compared to off-axis irradiation can be explained as follows (for details, see Raineri *et al.*[26] and Schrempel *et al.*[31]). In the case of the irradiation along a low index crystallographic direction, the defect distribution consists of three components: random, channeled, and dechanneled fractions. The ions which are scattered at surface atoms of the crystal at large angles form the random fraction. The channeled fraction consists of ions, which are prevented from close collisions with the target atoms (channeling effect). Therefore the penetration range of these ions is increased and the irradiation-induced defects occur at larger depths compared to off-axis irradiation. However, the channeled ions experience multiple scattering by various defects and by vibrating lattice atoms until they are dechanneled. This way the dechanneled fraction is formed. The random and the channeled ions dominate the defect formation at very low fluences. With rising ion fluence, i.e., with increasing defect concentration, the dechanneling probability increases and the dechanneled component becomes the dominating fraction. Consequently, the peak shift is a function of the ion fluence which has been shown previously.[31]

As a result of these processes defects are created at depths which are still larger compared to the defect distribution caused by off-axis irradiation. However, the peak of the total distribution is shifted toward the surface with increasing ion fluence.

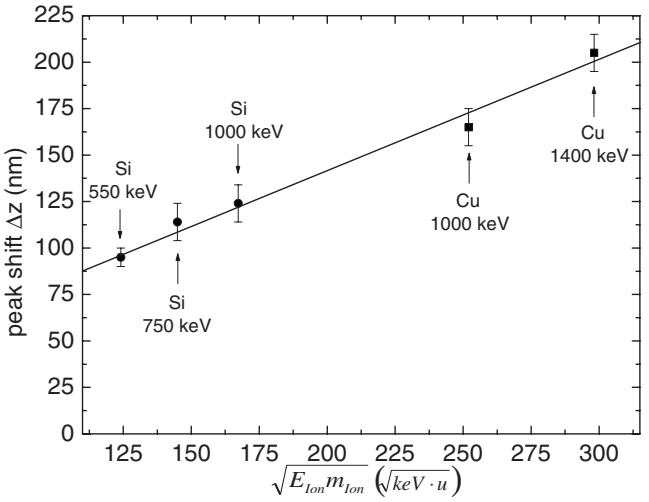

FIG. 4. Peak shift Δz as a function of the square root of the ion energy E_{ion} and ion mass m_{ion} for x-cut $LiNbO_3$ irradiated with different ion energies and ion species. Data were fitted by function (1) (solid line).

B. Effect of nuclear energy deposition

For the energy range where the nuclear energy deposition dominates the defect formation, Fig. 4 shows the measured shifts Δz from Table I as a function of the square root of both the ion energy and the ion mass. The peak shifts indicate a square-root dependence $\Delta z = A\sqrt{E_{\mathrm{ion}}m_{\mathrm{ion}}}$, with a fit parameter A which amounts to 0.60 ± 0.06 nm$\sqrt{(keVu)^{-1}}$ (solid line in Fig. 4).

Kerkow and Wedell[27] also found a square-root dependence of the peak shift, i.e., $\Delta z \propto \sqrt{E_{\mathrm{ion}}m_{\mathrm{ion}}}$, for on-axis irradiation of (110) and (111) silicon using Ca^+ and Mg^+ ions with different energies. Additionally, a dependence on the channel direction was determined. The shift of the damage distribution was explained qualitatively by a scattering model (see Kerkow and Wedell[27] and references therein) and Δz was given by the following analytical function:

$$\Delta z = \sqrt{\frac{E_{\mathrm{ion}}m_{\mathrm{ion}}}{E_d m}}D, \tag{1}$$

where E_d is the displacement energy, m is the mass of the target atom, and D is the average distance of the atomic strings forming the channels. Consequently the fit parameter A equates to $\sqrt{(E_d m)^{-1}}D$.

For Nb atoms, the parameter D was calculated to 9.2 Å, whereas E_d^{Nb} was assumed to be 25 eV and m^{Nb} amounts to 92.90 a.u. Hence, D is a reasonable value compared to the distances of the Nb atoms [lattice parameter (hexagonal): $a_H = 5.15$ Å and $c_H = 13.87$ Å].

C. Effect of electronic energy deposition

1. Defect formation due to electronic energy deposition

It can be clearly seen in Fig. 3(a) that the buried damage layer (area III) correlates with the maximum of the nuclear energy deposition ϵ_n (dotted line). Otherwise, the amorphous surface layer cannot be attributed to ϵ_n but to the high electronic energy loss ϵ_e, which occurs at the surface of the crystal (solid line).[22,36–38] The defects in the second area (II) occur as a result of an overlap of both energy losses.

Various theoretical models have been applied to describe the amorphization caused by electronic energy deposition, for instance, the thermal spike model as well as the Coulomb explosion model.[36–39] If the electronic energy deposition ϵ_e exceeds a material-specific threshold value $\epsilon_{e,\mathrm{th}}^{\mathrm{track}}$, each ion forms an amorphous track. With an increasing ion fluence, more and more ion tracks are formed until a continuous amorphous surface layer is produced due to multiple overlapping of tracks. In the case of $\epsilon_e < \epsilon_{e,\mathrm{th}}^{\mathrm{track}}$ the irradiation leads to the formation of point defects in the near-surface region, which accumulate to an amorphous layer with further irradiation. That is, the amorphous layer increases from the surface into the crystal with increasing ion fluence.[36,40,41] This implies an effective fluence-dependent threshold $\epsilon_{e,\mathrm{th}}(N_I)$ and suggests a cumulative effect (memory effect).[36,40,41] In experiments using high-energy irradiation (2.0–7.0 MeV) of $LiNbO_3$ the damage formation in the near-surface region due to electronic energy deposition was investigated.[22,36,42,43] Thereby the threshold $\epsilon_{e,\mathrm{th}}$ was determined for different ion fluences using the depth z of the boundary of the generated amorphous layer at which ϵ_e decreased from the value at the surface to the threshold $\epsilon_{e,\mathrm{th}}$. For example, for an ion fluence of 3×10^{14} cm^{-2}, which was used in our experiments, $\epsilon_{e,\mathrm{th}}(N_I)$ is in the range from 2 to 2.3 keV nm^{-1}. For the extrapolation to a "zero" ion fluence, i.e., one ion forms one amorphous track (single impact), a threshold $\epsilon_{e,\mathrm{th}}^{\mathrm{track}} = 5$ keV nm^{-1} was obtained. This value certified former experimental results concerning swift heavy-ion irradiation of $LiNbO_3$.[44]

Considering the electronic energy deposition ϵ_e for an ion energy of 2 MeV (see Table I) with the experimental results described above, it is obvious that $\epsilon_e > \epsilon_{e,\mathrm{th}}(N_I)$ for the used ion fluence of $N_I = 3 \times 10^{14}$ cm^{-2}, which is in accordance with the observed amorphous surface layer [see Fig. 3(a)]. By means of the thickness of the amorphous surface layer it is possible to determine $\epsilon_{e,\mathrm{th}}$ similar to Refs. 36, 40, and 41 (see Sec. IV C 2).

For both off- and on-axis irradiations [cf. Figs. 3(a) and 3(b)], the etching rate is higher in area I compared to area III which corresponds to a higher defect concentration in area I. Thus, the defect formation caused by electronic energy deposition is significantly higher in this energy range.

In contrast to the etching results, the defect distribution of the RBS spectra [cf. Fig. 2(b)] shows nearly commensurate defect concentration for all three areas. Thus, the areas II and III are only rudimentarily reflected in the RBS spectra, which can be accounted for by the disregarding of correlated defects by the calculation of defect profiles with DICADA (cf. Sec. III A). Hence, the etching rate is very sensitive to the defect concentration compared to the RBS measurements.

Simultaneously to the onset of defect formation at the crystal surface, the shift of the damage peak decreases for the Si^+ irradiations with $E > 1$ MeV (see Fig. 2). In Fig. 5 all measured peak shifts Δz for the Si^+ irradiations (cf. Table I) are depicted, whereas the dashed-dotted line represents the linear fit of Fig. 4 in Sec. IV B.

The decrease in the peak shift is connected with the damage formation due to the electronic energy deposition. On

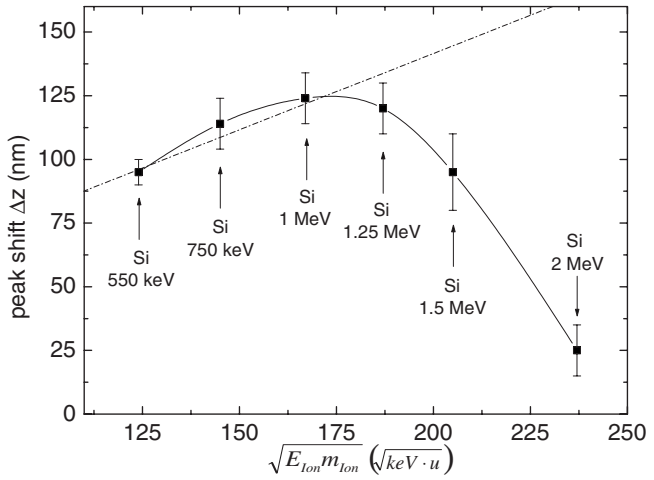

FIG. 5. Peak shift Δz as a function of the square root of the ion energy E_{ion} and ion mass m_{ion} for x-cut $LiNbO_3$ irradiated with Si^+ ions with different ion energies. The dashed-dotted line represents the linear fit in Fig. 4 Sec. IV B by Eq. (1).

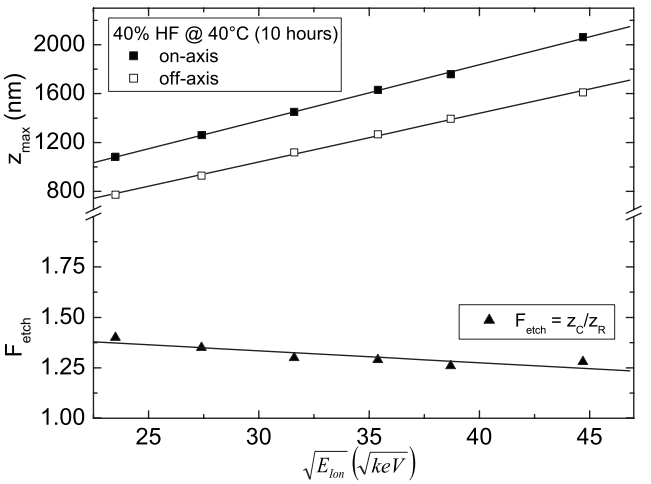

FIG. 6. Maximum etched depth $z_{\max}$ after etching in 40% HF solution for 10 h at a temperature of 40 °C for on- and off-axes Si^+ irradiation of x-cut $LiNbO_3$ at different ion energies. Additionally, the factor $F_{\text{etch}}=z_C/z_R$ is shown.

one hand, the defect formation caused by electronic energy deposition is significantly higher as stated above, and on the other hand the maximum of the defect formation is located close to the surface. Hence, with rising ion fluence the ions experience more and more multiple scattering by the resulting defects until they are dechanneled (cf. Sec. IV A, dechanneled fraction). Finally, the near-surface region is heavily damaged, all channels are destroyed, and an amorphous surface layer is formed. As a consequence the ions behave like off-axis incident ions and the defects are formed in the same depth as for off-axis irradiation (cf. Fig. 2 as well as Fig. 3). Hence, at the beginning of the on-axis irradiation where the surface of the crystal is still free of defects, the defects of the fourth area were formed. They have to be attributed to the defect formation caused by well-channeled ions (cf. Sec. IV A, channeled fraction and Schrempel *et al.*[31]).

2. Calculation of the threshold and electronic energy deposition

As mentioned above, it is possible to determine the threshold $\epsilon_{e,\text{th}}$ by means of the thickness of the amorphous surface layer which becomes evident in the etching process [see Fig. 3(a)]. The layer thickness is determined by the rapid decrease in the formerly high-constant etching rate at a depth of 275 nm [as indicated by the vertical dashed-dotted line in Fig. 4(a)]. At this depth the calculated electronic energy loss amounts to 200 eV $Å^{-1}$. The threshold $\epsilon_{e,\text{th}}(3\times10^{14}\ \text{cm}^{-2})$ $=200$ eV $Å^{-1}$ is in good agreement with the above-mentioned fluence-dependent threshold $\epsilon_{e,\text{th}}(N_I)$.

Note, for the determination of this threshold the nuclear energy loss is negligible because the electronic energy deposition dominates the defect formation in this energy range [cf. Fig. 3(a)]. Hence, the influence of ϵ_n is insignificant and does not sway the thickness of the amorphous layer, which is used for the determination.

For on-axis irradiation it was shown that the damage formation due to electronic energy loss starts at higher-ion energies compared to off-axis irradiation which can be accounted for by the lower electronic density in the channels.[26,31] As a consequence the electronic energy loss is reduced and the threshold for on-axis irradiation is exceeded just at higher-ion energies. The reduced electronic energy loss under channeling conditions ϵ_e^C can be determined in two ways. ϵ_e^C can be estimated by the ratio of the thickness of the amorphous surface layer z_a of on- and off-axis irradiations (see Fig. 4, area I) because $z_a \propto \epsilon_e$.[36,40,41] It follows that the electronic energy loss of the channeled ions ϵ_e^C irradiated along the $[11\bar{2}0]$ axis amounts to $0.73\epsilon_e^R$ $(z_a^C/z_a^R=0.73$ $=\epsilon_e^C/\epsilon_e^R)$. According to its various trajectories, the channeled ions experience not the same electron density so that this value relates to an average value.

Alternatively, ϵ_e^C can be estimated from the maximum range $R_{\max}$ of the impinging ion. The maximum etched depth $z_{\max}$ is correlated with $R_{\max}$, which is mainly determined by electronic energy loss $(z \propto R \propto 1/\epsilon_e)$.[26] Consequently, ϵ_e^C can be estimated by the ratio of the maximum etched depths z_C/z_R. Figure 6 shows the maximum etched depth $z_{\max}$ for on- and off-axis irradiated x-cut $LiNbO_3$ with Si^+ ions as well as the factor $F_{\text{etch}}=z_C/z_R$ as a function of the square root of the ion energy.

The maximum etched depths z_C and z_R were determined after 10 h etching in 40% HF solution at a temperature of 40 °C. With rising ion energy the maximum etched depth increases linearly for on- and off-axis irradiations. Compared to off-axis irradiation the maximum etched depth of on-axis irradiation is always clearly higher for all ion energies used. This behavior is reflected in the factor F_{etch}, which is always greater than 1 despite a slightly decrease from 1.4 (E_{ion} $=500$ keV) to 1.3 ($E_{\text{ion}}=2$ MeV). On the basis of the relation $z_C/z_R=F_{\text{etch}}=\epsilon_e^R/\epsilon_e^C$ and the mean value of $F_{\text{etch}}=1.35$ it is obvious that the electronic energy loss in channeling conditions is also reduced by a factor of 0.74. Using these two methods we found a 0.735 times lower average electronic energy deposition for channeling along the $[11\bar{2}0]$ axis of $LiNbO_3$ compared to off-axis irradiation.

V. CONCLUSIONS

The influence of ion energy and ion species on the defect formation in on-axis irradiated x-cut $LiNbO_3$ was investigated. It has been shown that in the energy range where the nuclear energy deposition dominates, the defect distribution for on-axis irradiation is shifted to larger depths. The peak shift increases linearly with the square root in both ion energy and ion mass. With further rising ion energy, e.g., Si^+ irradiation with $E>1$ MeV, the electronic energy loss becomes more and more dominant. When the electronic energy loss exceeds a material-specific threshold which could be estimated to 200 eV $Å^{-1}$, a strong damaged surface layer was observed whereas the peak shift nearly disappeared. These processes are a consequence of the defect formation due to the electronic energy deposition.

Furthermore, by comparing on- and off-axis irradiations with ion energies ranging from 1.0 to 2.0 MeV it was shown that the damage formation due to electronic energy deposition starts for on-axis irradiation just at higher energies. This effect is accounted for by the reduced electronic density in the channels. Consequently the electronic energy deposition is reduced for channeled ions and could be determined in two ways: by comparing the thickness of the amorphous surface layer as well as the maximal etched depths. Compared to the electronic energy loss for off-axis irradiation, the electronic energy loss under channeling conditions is reduced by a factor of ≈ 0.735.

With respect to the patterning of $LiNbO_3$ by means of ion-beam enhanced etching, the channeling irradiation offers the possibility to produce structures aligned with the crystal axis. However, metal masks with high-dimensional accuracy, which are required to pattern the sample with desired arrangement of structures, can only be produced with thicknesses below 400 nm. Thus, on-axis irradiation enables an increase in the depth of the pattern (approximately 1.35 times for x axis) without being obliged to increase the mask thickness due to the use of higher-ion energies.

[1] R. Weis and T. Gaylord, Appl. Phys. A **37**, A191 (1985).
[2] P. Leech and M. Ridgway, J. Vac. Sci. Technol. A **17**, 3358 (1999).
[3] D. Hines and K. Williams, J. Vac. Sci. Technol. A **20**, 1072 (2002).
[4] S. Yin, Microwave Opt. Technol. Lett. **22**, 396 (1999).
[5] F. Lacour, N. Courjal, M. Bernal, A. Sabac, C. Bainier, and M. Spajer, Opt. Mater. (Amsterdam, Neth.) **27**, 1421 (2005).
[6] I. Barry, G. Ross, P. Smith, R. Eason, and G. Cook, Mater. Lett. **37**, 246 (1998).
[7] I. Barry, G. Ross, P. Smith, and R. Eason, Appl. Phys. Lett. **74**, 1487 (1999).
[8] K. Mizuuchi, K. Yamamoto, and T. Taniuchi, Electron. Lett. **26**, 1992 (1990).
[9] F. Laurell, J. Webjorn, G. Arvidsson, and J. Holmberg, J. Lightwave Technol. **10**, 1606 (1992).
[10] H. Lee and S.-Y. Shin, Electron. Lett. **31**, 268 (1995).
[11] M. Kawabe, M. Kubota, K. Masuda, and S. Namba, J. Vac. Sci. Technol. **15**, 1096 (1978).
[12] G. Götz and H. Karge, Nucl. Instrum. Methods Phys. Res. **209-210**, 1079 (1983).
[13] C. Ashby, G. Arnold, and P. Brannon, J. Appl. Phys. **65**, 93 (1989).
[14] T. H. Shao, X. Y. Jiang, W. Shang, and X. Q. Feng, Mater. Sci. Eng., B **10**, 19 (1991).
[15] D. Gill, D. Jacobson, C. Whithe, C. Jones, Y. Shi, W. Minford, and A. Harris, J. Lightwave Technol. **22**, 887 (2004).
[16] F. Schrempel, T. Gischkat, H. Hartung, E.-B. Kley, W. Wesch, and A. Tünnermann, Mater. Res. Soc. Symp. Proc. 908E, 0908-OO16-01.1 (2006).
[17] F. Schrempel, T. Gischkat, H. Hartung, E.-B. Kley, and W. Wesch, Nucl. Instrum. Methods Phys. Res. B **250**, 164 (2006).
[18] G. Destefanis, P. Townsend, and J. Gailliad, Appl. Phys. Lett. **32**, 293 (1978).
[19] P. Townsend, Nucl. Instrum. Methods Phys. Res. B **46**, 18 (1990).
[20] A. Kling, M. da Silva, J. Soares, P. Fichtner, L. Amaral, and F. Zawislak, Nucl. Instrum. Methods Phys. Res. B **175-177**, 394 (2001).
[21] A. Meldrum, L. Boatner, W. Weber, and R. Ewing, J. Nucl. Mater. **300**, 242 (2002).
[22] G. Bentini, M. Bianconi, L. Correra, M. Chiarini, P. Mazzoldi, C. Sada, N. Argiolas, M. Bazzan, and R. Guzzi, J. Appl. Phys. **96**, 242 (2004).
[23] J. Barrett, Phys. Rev. B **3**, 1527 (1971).
[24] D. Morgan, *Canneling-Theory, Observation and Application* (Wiley, New York, 1973).
[25] D. Gemmell, Rev. Mod. Phys. **46**, 129 (1974).
[26] V. Raineri, V. Privitera, G. Galvagno, F. Priolo, and E. Rimini, Mater. Chem. Phys. **38**, 105 (1994).
[27] H. Kerkow and R. Wedell, Radiat. Eff. Defects Solids **125**, 147 (1993).
[28] M. Posselt, M. Mäder, R. Grötzschel, and M. Behar, Appl. Phys. Lett. **83**, 545 (2003).
[29] B. Pipeleers, S. Hogg, and A. Vantomme, J. Appl. Phys. **98**, 123504 (2005).
[30] Z. Zolnai, A. Ster, N. Khanh, G. Battistig, T. Lohner, J. Gyulai, E. Kotai, and M. Posselt, J. Appl. Phys. **101**, 023502 (2007).
[31] F. Schrempel, T. Steinbach, T. Gischkat, and W. Wesch, Nucl. Instrum. Methods Phys. Res. B **266**, 2958 (2008).
[32] J. Ziegler, J. Biersack, and U. Littmark, *The Stopping and Range of Ions in Solids* (Pergamon, New York, 2003).
[33] K. Gärtner, Nucl. Instrum. Methods Phys. Res. B **227**, 522 (2005).
[34] K. Gärtner, Nucl. Instrum. Methods Phys. Res. B **132**, 147 (1997).
[35] J. Reinisch, F. Schrempel, T. Gischkat, and W. Wesch, J. Electrochem. Soc. **155**, D298 (2008).
[36] F. Agulló-López, A. Mendez, G. García, J. Olivares, and J. M. Cabrera, Phys. Rev. B **74**, 174109 (2006).
[37] M. Toulemonde, C. Dufour, A. Meftah, and E. Paumier, Nucl. Instrum. Methods Phys. Res. B **166-167**, 903 (2000).

[38] A. Meftah, J. M. Constantini, N. Khalfaoui, S. Boudjadar, J. P. Stoquert, F. Studer, and M. Toulemonde, Nucl. Instrum. Methods Phys. Res. B **237**, 563 (2005).
[39] R. Fleischer, P. Price, and R. J. Walker, J. Appl. Phys. **36**, 3645 (1965).
[40] J. Olivares, G. García, F. Agulló-López, F. Agulló-Rueda, A. Kling, and J. Soares, Appl. Phys. A: Mater. Sci. Process. **81**, 1465 (2005).
[41] F. Agulló-López, G. García, and J. Olivares, J. Appl. Phys. **97**, 093514 (2005).
[42] G. G. Bentini, M. Bianconi, M. Chiarini, L. Correra, C. Sada, P. Mazzoldi, N. Argiolas, M. Bazzan, and R. Guzzi, J. Appl. Phys. **92**, 6477 (2002).
[43] M. Bianconi, N. Argiolas, M. Bazzam, G. G. Bentini, M. Chiarini, A. Cerutti, P. Mazzoldi, G. Pennestri, and C. Sada, Nucl. Instrum. Methods Phys. Res. B **249**, 122 (2006).
[44] B. Canut, S. Ramos, R. Brenier, P. Thevenard, J. Loubet, and M. Toulemonde, Nucl. Instrum. Methods Phys. Res. B **107**, 194 (1996).